Registration and 3D Visualization of Large Microscopy Images

Kishore Mosaliganti[a], Tony Pan[b], Richard Sharp[a], Randall Ridgway[a], Srivathsan Iyengar[b], Alexandra Gulacy[b], Pamela Wenzel[c], Alain de Bruin[c], Raghu Machiraju[a], Kun Huang[b], Gustavo Leone[c] and Joel Saltz[b]

[a]Computer Science and Engineering,
[b]Biomedical Informatics,
[c]Human Cancer Genetics Program, The Ohio State University;

ABSTRACT

Inactivation of the retinoblastoma gene in mouse embryos causes tissue infiltrations into critical sections of the placenta, which has been shown to affect fetal survivability. Our collaborators in cancer genetics are extremely interested in examining the three dimensional nature of these infiltrations given a stack of two dimensional light microscopy images. Three sets of wildtype and mutant placentas was sectioned serially and digitized using a commercial light microscopy scanner. Each individual placenta dataset consisted of approximately 1000 images totaling 700 GB in size, which were registered into a volumetric dataset using National Library of Medicine's (NIH/NLM) Insight Segmentation and Registration Toolkit (ITK). This paper describes our method for image registration to aid in volume visualization of tissue level intermixing for both wildtype and Rb^{-} specimens. The registration process faces many challenges arising from the large image sizes, damages during sectioning, staining gradients both within and across sections, and background noise. These issues limit the direct application of standard registration techniques due to frequent convergence to local solutions. In this work, we develop a mixture of automated and semi-automated enhancements with ground-truth validation for the mutual information-based registration algorithm. Our final volume renderings clearly show tissue intermixing differences between both wildtype and Rb^{-} specimens which are not obvious prior to registration.

Keywords: Registration, Light Microscopy, Image Processing

1. INTRODUCTION

Many human diseases have genetic bases that manifest phenotypically as functional and/or structural deficiency. The retinoblastoma (Rb) gene was the first tumor suppressor gene found to be associated with a specific cancer, and has been studied extensively in both human cells and mouse models. Recently, it has been shown that inactivation of the Rb gene in mouse embryos results in morphological changes in the placenta, including reduction in vascularity of the labyrinth layer. Mouse placentae are composed of three distinct embryonic cell types that aggregate in layers: labyrinth, spongiotrophoblast, and glycogen. Figure 1a shows a sample slide with the labyrinth, spongiotrophoblast and glycogen layers marked in red, yellow and blue boundaries, respectively. The

---

Further author information: (Send correspondence to Kishore Mosaliganti)
Kishore Mosaliganti: E-mail: mosaligk@cse.ohio-state.edu, Telephone: 1 614 292 4029
Tony Pan: E-mail: tpan@bmi.ohio-state.edu, Telephone: 1 614 292 1157
Richard Sharp: E-mail: sharpr@cse.ohio-state.edu, Telephone: 1 614 292 4029
Randall Ridgway: E-mail: ridgwayr@cse.ohio-state.edu, Telephone: 1 614 292 4029
Alexandra Gulacy: E-mail: gulacy@bmi.osu.edu, Telephone: 1 614 688 5430
Srivathsan Iyengar: E-mail: iyengar.8@osu.edu, Telephone: 1 614 294 2644
Pamela Wenzel: E-mail: Pamela.Wenzel@osumc.edu, Telephone: 1 614 292 2459
Alain de Bruin: E-mail: alain.debruin@osumc.edu, Telephone: 1 614 292 3817
Raghu Machiraju: E-mail: raghu@cse.ohio-state.edu, Telephone: 1 614 292 6730
Gustavo Leone: E-mail: Gustavo.Leone@osumc.edu, Telephone: 1 614 688 4567
Joel Saltz: E-mail: joel.saltz@osumc.edu, Telephone: 1 614 292 4029

Medical Imaging 2006: Image Processing, edited by Joseph M. Reinhardt, Josien P. W. Pluim,
Proc. of SPIE Vol. 6144, 61442V, (2006) · 0277-786X/06/$15 · doi: 10.1117/12.653505

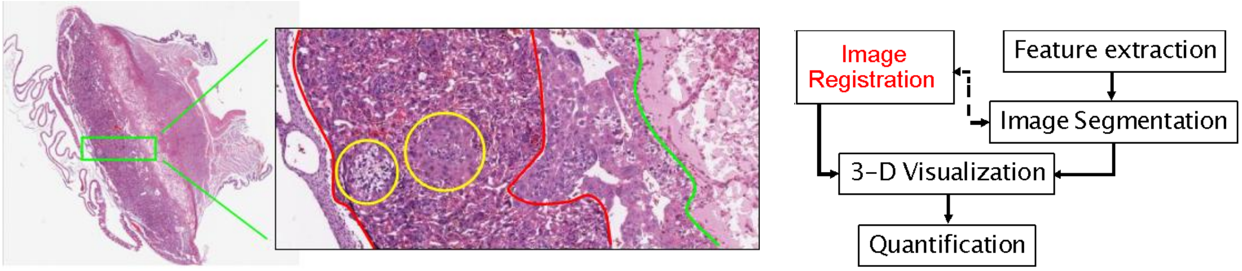

(a) (b)

Figure 1. (a): An example of one of the Rb^{-} histological mouse placenta slides showing different tissue types. A small region magnified to show labyrinth layer (within red boundaries), spongiotrophoblast layer (between the red and green boundaries) and spongiotrophoblast and glycogen infiltrations (yellow circles). (b): Overview of the image analysis framework

labyrinth layer serves the critical function of gas, nutrient, and waste exchange between the mother and the fetus. Decrease in vascularity is thought to contribute to fetal death at 14.5 days of gestation.[1]

For this study, hematoxylin and eosin stained serial sections of wildtype and mutant placenta were digitized in a light microscopy scanner to obtain high resolution color images. Image analysis of the structural changes in mouse placenta provides an opportunity for quantitative correlation of genetic changes with phenotype expressions. Specifically, the goals of image analysis are segmentation of the tissue layers, interface visualization, and quantitative measurement of volume and surface area of the layers. Registration of the tissue sections is an important pre-processing step for various algorithms as shown in Figure 1b, and its accuracy directly affects the quantification and interpretation of the results.

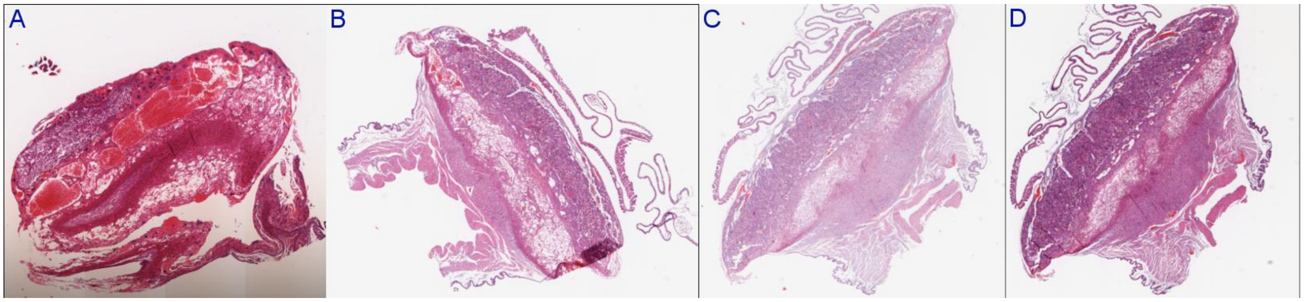

Figure 2. Images drawn from the 04-2069 placenta sectioned at $3\mu m$ thickness. A: background noise from acquisition. B: tissue fold with some tear and shear. C,D: consecutive sections have non-linear intensity variations.

Three sets of wildtype and mutant (Rb^{-}) placenta were harvested at 13.5 days of gestation and prepared using a standard histological protocol. They were fixed in formalin, embedded in paraffin and sectioned at $5\mu m$ thickness using a microtome. The 04-2069 and 04-4351 placentae were sectioned at $3\mu m$ thickness. Serial sections were mounted on glass slides and stained with hematoxylin and eosin. The slides are scanned in an Aperio ScanScope slide digitizer at 200x magnification. The image dimensions on average were (15K x 15K x 3). Each placenta dataset produced approximately 600-800 color images, ranging in size from 300GB to 500 GB. Figure 3a tabulates the placenta datasets with the corresponding number of slices and file size on disk. The manual nature of the tissue preparation process introduces the following types of artifacts, which required additional preprocessing as well as modifications to the registration process:

- *Orientation differences*: Sections are mounted in different orientations on glass slides due to the manual nature of the process.
- *Luminance gradient*: Sections mounted close to the edge of the glass slide produce images with significant luminance gradients (Figure 2A).
- *Non-tissue noise*: Dust and air bubbles in the slide may cause artifacts.
- *Damaged and missing sections*: During sectioning and mounting, sections are occasionally torn, folded, or discarded entirely (Figure 2B).
- *Staining variations*: Differences in section thickness, staining duration, and stain concentration results in color variations in histologically stained specimens. Tissue boundaries are difficult to recognize when these staining variations are present (Figure 2C,D).

Improvements to the tissue preparation process prior to scanning were made in order to make the images more consistent in terms of orientation and position of the tissue on the slide. Later placenta samples were sectioned at 5 mum (instead of 3 μm) to correct the high incidence of damage and excessive shearing. Staining of all slides from the same placenta was conducted at the same time to reduce color variation. Furthermore, staining of all slides immediately after sectioning was done to reduce dryness and cracking of the tissue, etc. These efforts led to considerable improvements in the quality of the images prior to the pre-processing techniques. Nevertheless, the images still required processing for achieving high accuracy in the quantification.

We utilize pre-processing techniques to account for acquisition artifacts, defective histology sections, and large parameter search space. We employ a multi-resolution implementation of the rigid mutual-information registration algorithm with a new optimization strategy based on a randomized search perturbation. Thus, we obtain robust registration of a given dataset. The rest of the paper is organized as follows. In Section 2, we describe related work in registration and reconstruction of 3D medical datasets. In Section 3, we motivate and describe our pre-processing tools that aid registration and reduce manual intervention. We employed mutual information registration from National Library of Medicine's (NIH/NLM) Insight Segmentation and Registration Toolkit (ITK),[2] which is an open-source, cross-platform software toolkit. In Section 4, we detail our approach towards enhancing registration performance by using a hybrid optimization strategy. We provide 3D visualizations and numerical results to demonstrate our improvements in Section 5.

2. RELATED WORK

Below we discuss previous work that have considered similar problems in registration, segmentation and 3D reconstruction. Johnson and Christensen[3] present a hybrid landmark/intensity-based deformable registration technique. The approach uses an iterative process of first registering landmarks independently of intensity, then attempts to minimize image intensity difference independent of landmarks. In Chui *et al*,[4] manually extracted sulcal points, located on the outer cortical surface, were spatially normalized via a robust point matching algorithm thus achieving non-linear matching of the brains. While these approaches[3–5] are useful for mapping 2D brain sections to brain-atlases, this approach would not work well on our data. First, it is not obvious from the unclassified data what constitutes a landmark point, let alone the challenge of manually marking landmarks for thousands of placenta slices. Furthermore, we are interested in the original 3D shape of the placenta.

In the mouse placenta, the deformation among successive slices remains primarily a rigid transformation, with minor amounts of shear. While this work focusses on rigid models, we are also currently exploring the use of deformable methods to obtain higher orders of alignment. Ideally, a placenta atlas or a model would provide us a way to uniformly align each slice to the model. Alternatively, finite element based techniques also appear promising. Deformable registration techniques[6–8] involving contour or feature matching in successive slices will corrupt the overall 3D shape and possibly the intermixing of the tissues.

Arganda-Carreras *et al*[9] present a method for automatic registration of histology sections. The authors present two techniques for non-deformable registration using Sobel transforms and segmentation contours. Leung and Malik *et al*[10] use the powerful cue of contour continuity is exploited by providing curvilinear groupings into region-based image segmentation. The approach obtains soft contour information through an orientation energy metric that has been proposed in the literature. Weak contrast gaps and subjective contours are completed by contour propagation. Our data does not however have well defined contours on a slice by slice basis. Thus, contour based registration techniques[9–12] fail on our dataset.

Ourselin *et al*[13] also present a technique for 3D reconstruction based on histology slices. Their work mostly focuses on block matching registration techniques which are demonstrated on both rat and rhesus monkey brain slices. Our microscopy images are much nosier and have more artifacts than brain histology slices. Furthermore our goal is to identify intermixing of layers, not just reconstruct the three dimensional shape. We now describe the preprocessing algorithms that we employ prior to the registration.

3. PREPROCESSING METHODS

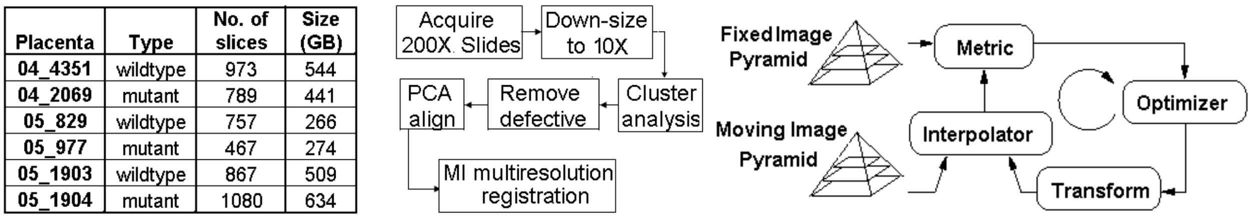

Placenta	Type	No. of slices	Size (GB)
04_4351	wildtype	973	544
04_2069	mutant	789	441
05_829	wildtype	757	266
05_977	mutant	467	274
05_1903	wildtype	867	509
05_1904	mutant	1080	634

(a) (b) (c)

Figure 3. (a): Table showing the placenta datasets with the corresponding number of images and dataset sizes. (b): Pre-processing pipeline. (c): ITK-based registration framework. Transforms are scaled when passed from a lower to higher resolution.

The overall framework for placenta images includes 5 steps: yolk-sac removal, tissue detection, defective section exclusion, PCA alignment, and mutual information registration with perturbation-based search optimization. Figure 3b provides a flowchart of the preprocessing tasks prior to registration. For clarity, illustrations are presented along with the algorithm descriptions.

3.1. Yolk-sac Removal

Nearly every slice of the placenta contains yolk-sac tissue (the wispy features near the bottom of the slide). Since the presence of yolk-sac tissue can significantly distort during the section mounting process, we find that this tissue is oriented differently on nearly every slide in the volume. This complicates the registration process since the yolk-sac cannot be rigidly registered to reconstruct its original three-dimensional shape. Attempts at automatic removal of the yolk-sac were not successful due to its complex and random structure across slides and across specimens. Instead we manually remove the yolk-sac from every slice before the register and volume render step.

3.2. Tissue Detection

The first step separates the tissue (foreground) from the background. Histology images, unlike radiology images, usually have background pixels with high luminance values. During registration, a moving image may be transformed such that a background pixel falls outside of the bounds of the stationary image (Figure 6). In this case, the high background luminance may significantly affect the metric value and decrease registration accuracy. We limit registration to use only tissue pixels, which also reduce errors due to luminance gradients.

We use a clustering-based approach for tissue detection, as it performs well in the presence of luminance gradient, background noise, and staining variations when compared to global thresholding with or without histogram equalization. Figures 4a and 4b show the differences between global thresholding and clustering approaches for the image in Figure 2A. Images were clustered using the well-established k-means algorithm with $k = 2$. We implemented the k-means algorithm with multi-resolution kd-tree optimizations, based on the work of Bradley and Fayyad *et al.*[14] On 10x images, the optimized clustering on average took 3-4s per image. Tissue pixels are identified and stored as binary masks which are used in the exclusion of defective sections and the PCA alignment of sections.

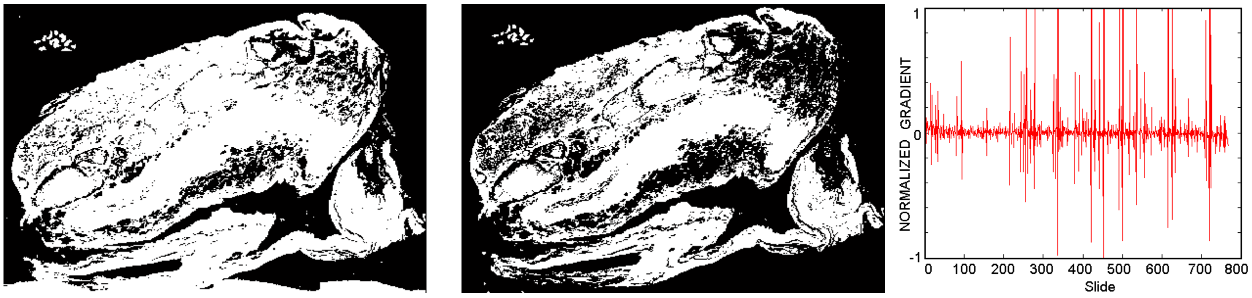

(a) (b) (c)

Figure 4. (a) Foreground separation using the global thresholding approach. (b) Foreground separation using the k-means. (c) Normalized area gradient plot to set thresholds for identifying defective section locations.

3.3. Defective Section Exclusion

To improve robustness, defective sections need to be identified and excluded from the registration process. We leverage the knowledge that all images are acquired at the same magnification, thus tissue sizes in successive images should not change significantly. Large tissue size variations are likely due to broken, or folded sections. Using the binary masks from Section 3.2, foreground areas were computed for each image and plotted against section position (Figure 4b. Spikes in the plot indicate potentially defective sections. Figure 4c shows the difference in foreground area between an image and its predecessor, normalized with its foreground area. Of a total of 789 slides, 173 potentially defective sections were identified by thresholding the absolute value of normalized area in the 04-2069 mutant placenta. A value of 0.03 was found to be suitable. Visual inspection confirmed that 70 of these sections were truly defective. An additional 33 sections were not identified by area measurement although they suffer from defects including background noise. These were identified after registration during 3D visualization stage, and their neighbors were re-registered. The automation reduced the number of images that require manual inspection prior to registration from 786 to 173.

3.4. PCA Alignment

Tissue orientations presents a significant challenge in the registration of histology images. Unlike radiology images, where the patient orientation is well known, histology sections can be mounted in any orientation on the glass slides. The possible translations and rotations in a plane define the *transform space* for the placenta images. For a pair of images, the transform space is searched based on the *learning rates* in the optimization framework to find an optimal transform. The variable orientation requires different learning rates for different image pairs. High learning rates are suitable for image pairs with widely different orientations. However, the same high learning rates also overshoot the global solution for similarly oriented image pairs resulting in convergence to local minima. Low learning rates, on the other hand, do not allow the optimizer to escape from local minima for pairs with dissimilar orientations. Hence, setting a single learning rate for all image pairs is not practical.

Using *a priori* knowledge that mouse placenta sections are typically elongated in shape, we use principle component analysis (PCA) to estimate tissue orientation. The orientations are used to initialize registration, thus restricting the transform search space. This allows more uniform learning rates and increases the likelihood of converging closer to the global optima. PCA is performed for each tissue mask image. The orientation angles are used to rotate and align the original histology images. Figure 5a shows the same two sequences of images before and after PCA alignment. Figure 5b shows the mutual information (MI) metric of registration using the original sequence (blue) and the PCA-aligned sequence (red), plotted against section number. The MI values indicate that PCA alignment significantly improves the registration. Although PCA alignment does not completely remove the occurrence of local solutions, the improvements do indicate that PCA initialized registration tends to produce local solutions that are closer to the global optima.

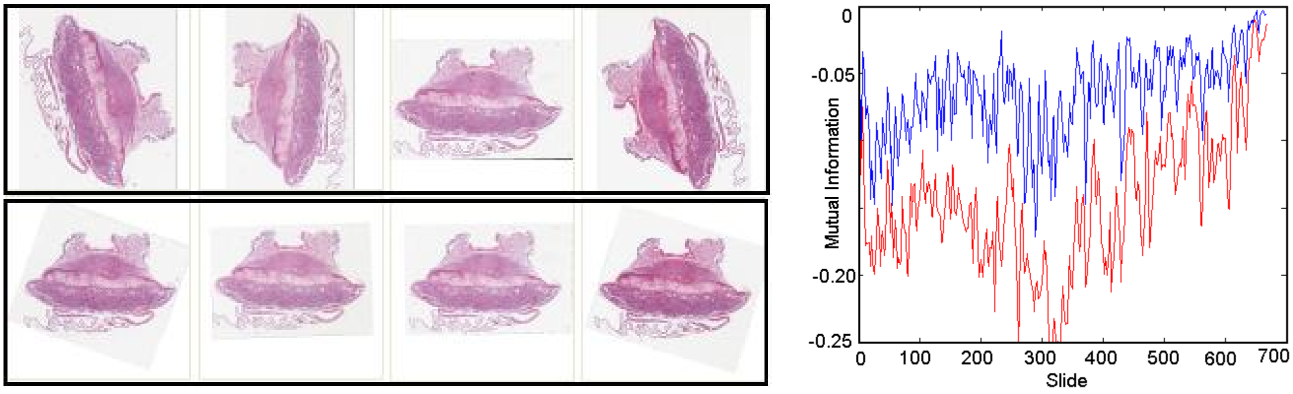

(a)

(b)

Figure 5. (a) Top sequence shows the initial random orientation of the placenta images drawn from the 04-2069 dataset. The bottom sequence shows PCA- aligned images. (b) Registration metric values after registration of original, unaligned images (blue) and PCA aligned images (red). Note that the negative of mutual information is plotted and lower numbers indicate better performance.

4. MUTUAL INFORMATION BASED REGISTRATION

We perform registration as an optimization process that searches for an image transform that allows the closest similarity between consecutive images. The input is a pair of stationary (S) and moving (M) images. The framework iteratively passes M through 4 stages: *transform*, *metric*, *optimizer*, and *interpolator* as shown in Figure 3c. At a given iteration, the *transform* stage applies transform T_n on M which is then resampled onto a grid in the *interpolator* stage to yield $T_n(M)$. The *metric* stage computes the quality of fit between S and $T_n(M)$. Based on the similarity metric values from current and prior iterations, the optimizer produces a refinement in transform T_{n+1}. At convergence, S and $T_n(M)$ have the optimal metric value thereby aligning the images. For the placenta dataset, we register each image to its predecessor, and the pairwise transforms were merged sequentially to obtain each image's global transform.

4.1. Registration Framework Components

We adopt the maximization of mutual information[15, 16] (MI) as our basis. MI based methods are effective in registering multi-modal images where pixel intensities between images are not linearly correlated. While the placenta images are acquired using the same protocol, they have multimodal characteristics due to staining variations and the occasional luminance gradients. Rigid body registration techniques requiring intrinsic point- or surface-based landmarks,[17] and intramodal registration methods[18] that relying on linear correlation of pixel values are inadequate under these conditions.

It has been shown that optimization scheme affects the final registration especially near convergence,[18] while linear interpolation provides reasonable accuracy. Therefore, we adopt bi-linear interpolation[15] and regular step gradient descent optimizer[19] in the *interpolator* and *optimizer* stages. We model the *transform* using rigid

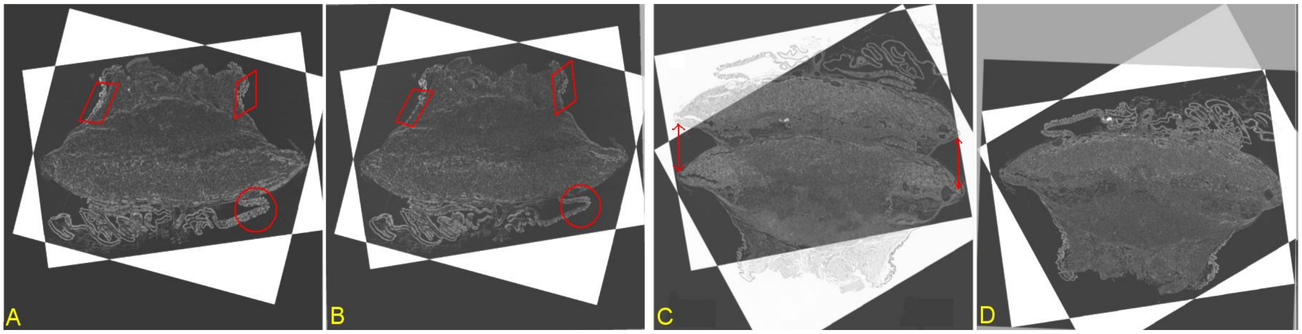

Figure 6. Application of the regular step gradient descent (A,C) and the two-level optimizer (B,D) on 2 slides drawn from the 04-2069 dataset that are initially aligned using PCA. Note that the regular step gradient descent settles in local solutions.

2D transform, which allows 2D rotation and translation. This choice is based on the physical conditions that the tissue does not elastically deform significantly during sectioning or mounting, that the microtome produces parallel sections, and that all images are acquired at the same magnification. While there is some amount of shear deformation during slicing, it remains insignificant compared to the rigid displacement and we chose to counter it as part of our future work. Remaining variable components of the transform are in-plane rotation and translation.

4.2. Multiresolution Registration

It has been shown[20] that MI registration with multiresolution strategies can achieve similar robustness compared to direct registration. Studholme[19] reported no loss in registration precision and significant computational speed-up when comparing different multiresolution strategies. We adopt the multiresolution approach, using 3-level image pyramids as shown in Figure 3c. The image magnifications used were 10x, 20x, and 50x. Optimal transforms obtained from a lower magnification (X_n) are scaled and used as initialization for registration of the next higher magnification (X_{n+1}). Registration is then performed on the X_{n+1} images, potentially with different optimizer parameters, to refine the transforms. The process is repeated for each magnification level to obtain the final transforms. We note that at magnifications higher than 50x, the computation cost for registration outweighs the improvements in accuracy.

4.3. Two-level Optimization

Tissue detection and PCA-based image alignment significantly improved registration performance by reducing the search space for the optimal transform. However, 3D visualization of the registered placenta revealed that the transforms remained suboptimal. Experiments with different optimizers such as conjugate-gradient and gradient descent did not affect performance significantly due to noisy metrics. We propose the use of a novel two-level optimization scheme by searching the transform space neighborhood with a random walk strategy.

4.3.1. Optimizer

Optimizers such as regular-step gradient descent and conjugate gradient[19] increase the rate of convergence by refining the transform based on their current learning rates from observed MI gradients. However, their performance degrades rapidly since the learning rates are sensitive to data noise. In the placenta dataset, we observe that ITK optimizers converge to local solutions as shown in Figure 6(A,C) for most image pairs (better MI values were later observed with the two-level optimizer).

We use a two-level optimization strategy, which perturbs converged solutions through random walks and then restarts the normal registration process. In essence, the perturbation introduces a step in the transform space that is larger than the specified learning rate of the regular step gradient descent optimizer. The step is a restricted translation and rotation around the PCA initialization. If the previous result was a local minimum, then the perturbation may result in a better solution with higher MI (lower negative MI) as shown in Figure 6

(B,D) and a new solution is realized. The process is repeated until the MI does not improve even after a user-defined, N, perturbations. Similar to standard optimizers, convergence to a global solution is not guaranteed. However, the registration is likely to perform better since this approach allows hill climbing against the gradient direction.

In the placenta images, we determined that maximum transform deviation of PCA aligned images is ± 80 pixels in translation and ± 10 degrees in rotation around the tissue centroid. The hybrid optimization strategy leads to global solutions in 99% of the images within N=20 iterations. The remaining 1% converges within N=50 iterations. Figure 7a shows the plots of the final MI values of all the images (blue) belonging to the 04-2069 dataset using the two-level optimizer. The improvement of the two-level optimizer compared to standard optimizer is shown as a difference in the MI values at convergence (red). The average MI of all images using the standard and two-level optimizers are -0.122 and -0.142 respectively. Figure 7b and 7c shows the 3D reconstruction of the placenta surface and the two-level optimizer. Owing to poor alignment in the standard case, the surface of the placenta appears broken and jagged. However, the two-level optimizer resulted in generation of a smoother surface.

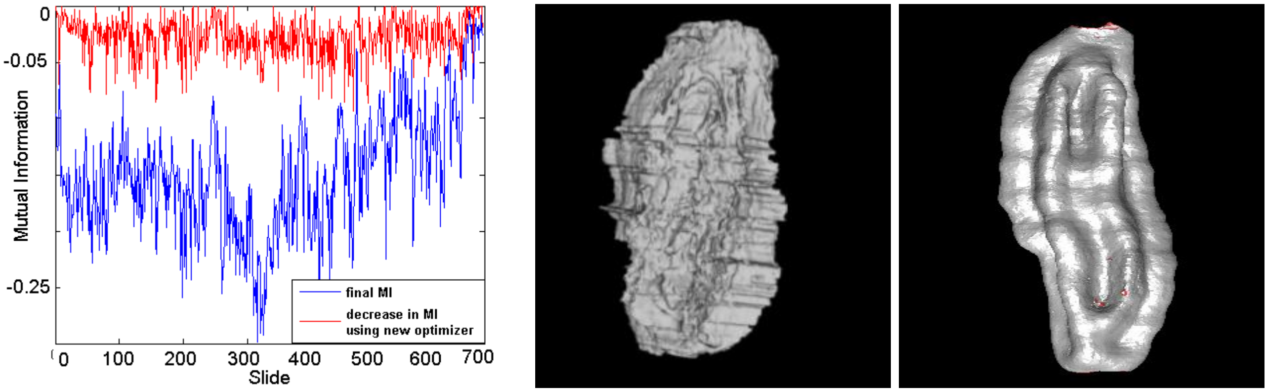

(a)

(b)

(c)

Figure 7. (a) Plot showing the metric values after convergence (blue) for all the image pairs in 04-2069 placenta. The improvement in metric values using the two-level versus the standard optimizer is also shown (red). Note that the negative of mutual information is plotted. (b) Surface reconstruction of the 04-2069 placenta using the registration from the standard ITK mutual information registration framework using regular step gradient descent optimizer. (c) using the hybrid optimizer.

5. RESULTS AND DISCUSSION

This section reports on a number of experiments we conducted to evaluate our methods. Our experiments were conducted using a set of 10 image pairs drawn randomly from each of the 6 placenta datasets. Using these image pairs as the basis, we test the output of the 2 step optimizer and note its performance over manually registered images by measuring the mutual information metric in both the instances. Note that manual registration may yield a solution very close to the optimal solution since it is based on a number of cues such as visible landmarks including matching blood vessels, contour curvatures, etc. Hence, manual registration results may be treated as ground-truth. Manual registration is accomplished by using a custom-built tool that permits the selection of a set of points interactively and develops a 2D transform.

Figure 8 shows the experimental results observed on two wildtype and two mutant placentas. Each bar graph tabulates the result on a particular placenta dataset. The x-axis represents the 10 image pairs and y-axis is the mutual information metric. The blue and red bars represent the two step optimizer and the manual methods respectively. From the results it is easy to observe that there is no statistically significant difference in the mutual

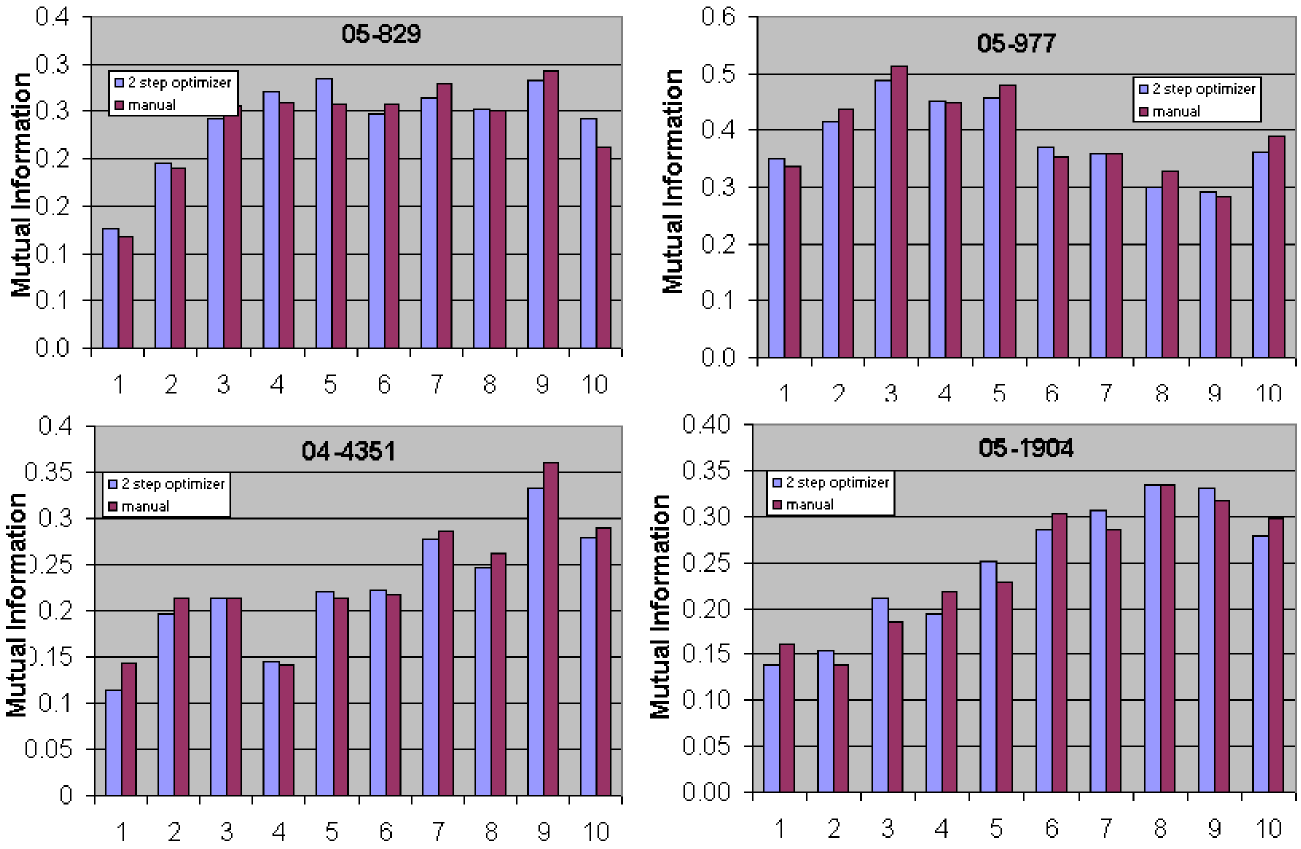

Figure 8. Validation of the registration achieved by the two step optimizer as compared to the manual registration of 10 image pairs drawn randomly from 4 placenta datasets namely 05-829, 05-977, 04-4351 and 05-1904.

information metric values when using the two step optimizer as against manual methods. In fact, in several cases, the two step optimizer seems to have resulted in a higher metric value than the manually registered case. The reason being that manual methods are based on aligning some landmarks. However, the image must have suffered some non-linear shear deformation during the slicing and mounting process. Hence, manual methods although more accurate lead to lower mutual information values. Is it possible for the two step optimizer to achieve a more closer values to the manual case?

The answer is yes, it is possible by allowing longer iteration times for the randomized walk strategy. However, the computational costs may outweigh the incremental improvements. Figure 9 shows the volume visualization of the stacked up images in 3D for 4 different placenta datasets. The images give us an idea of the 3D shape of the outer placenta. By superimposing segmented results on the registered volumes as in Figures 9e and 9f, it is possible for us to understand the intermixing of several placenta layers and to observe the infiltrations. This provides important information to the domain experts on understanding the structural differences between the wildtype and mutant placentas.

6. CONCLUSION AND FUTURE WORK

In this paper, we described our experience in registering large serial sections of a histology sample. Our contribution involves methods to adapt the ITK registration process for real-world data such as the mouse placenta. We utilized pre-processing techniques to account for acquisition artifacts, defective histology sections, and large parameter search space. We also employed a multi-resolution implementation of MI registration algorithm. As a result, manual intervention during registration is reduced significantly. We propose a new optimization strategy that has a higher probability of convergence to global solutions albeit with longer processing times. Our results

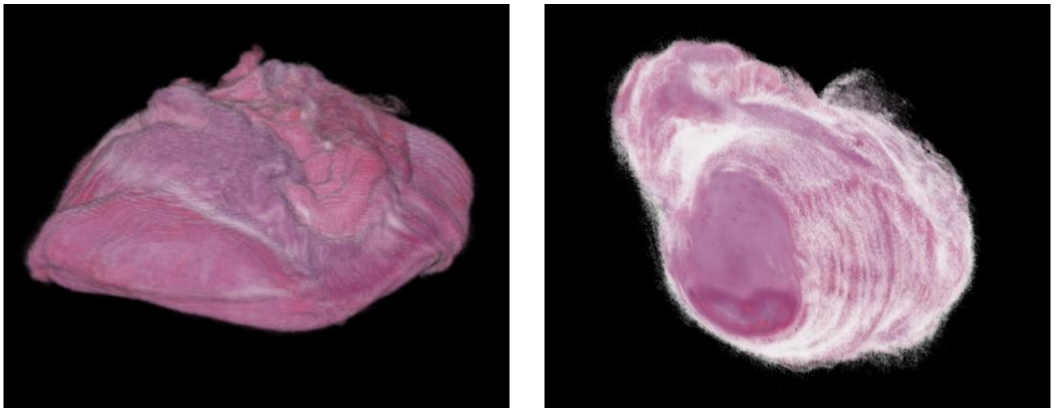

(a) 05-829 Wildtype placenta

(b) 05-997 Mutant placenta

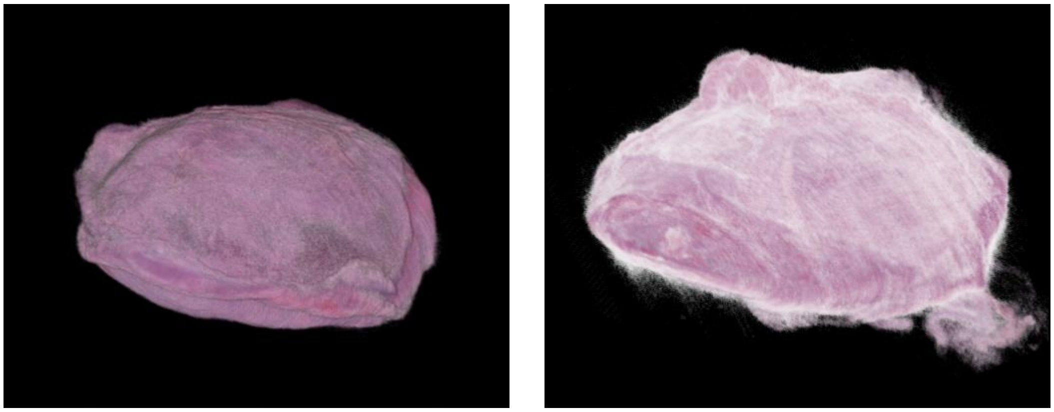

(c) 05-1903 Wildtype placenta

(d) 05-1904 Mutant placenta

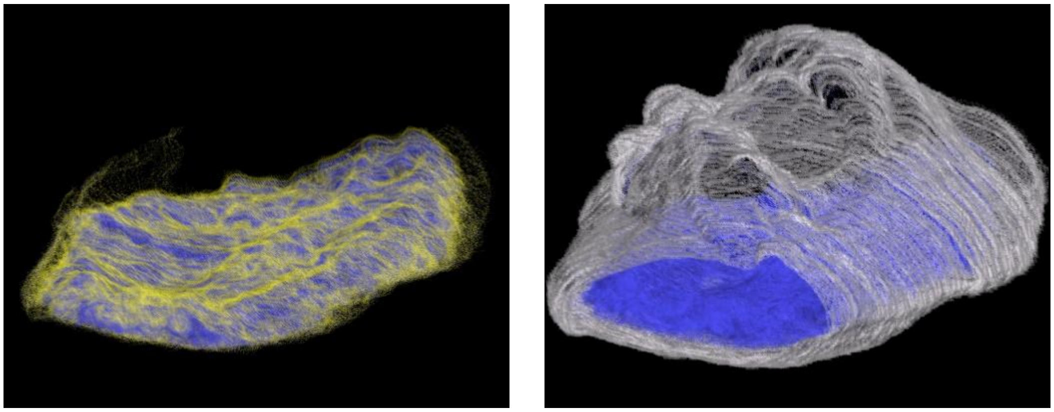

(e) 05-829 Labyrinth-Spongiotrophoblast intermixing

(f) 05-829 Overall perspective

Figure 9. Volume rendering of the stacked up RGB slices of the wildtype (05-829, 05-1903) and mutant (05-997, 05-1904) placentas. The bottom images show the intermixing in the 05-829 wildtype placenta tissue at the labyrinth-spongiotrophoblast interface and the overall position of the labyrinth layer in the volume.

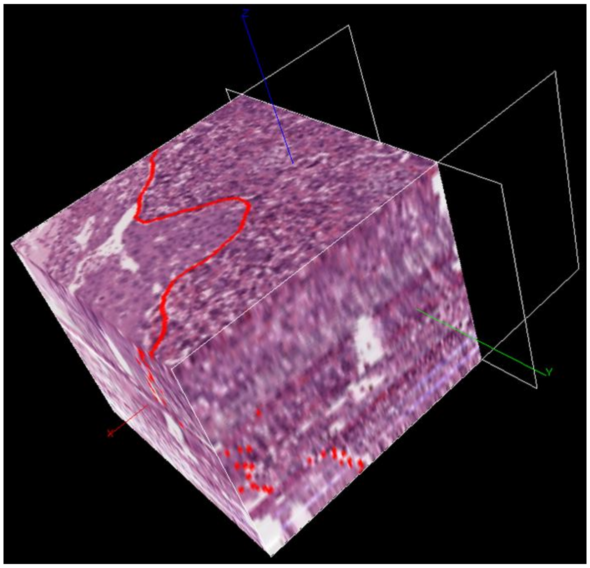

(a) 3D cube containing a finger-like infiltration

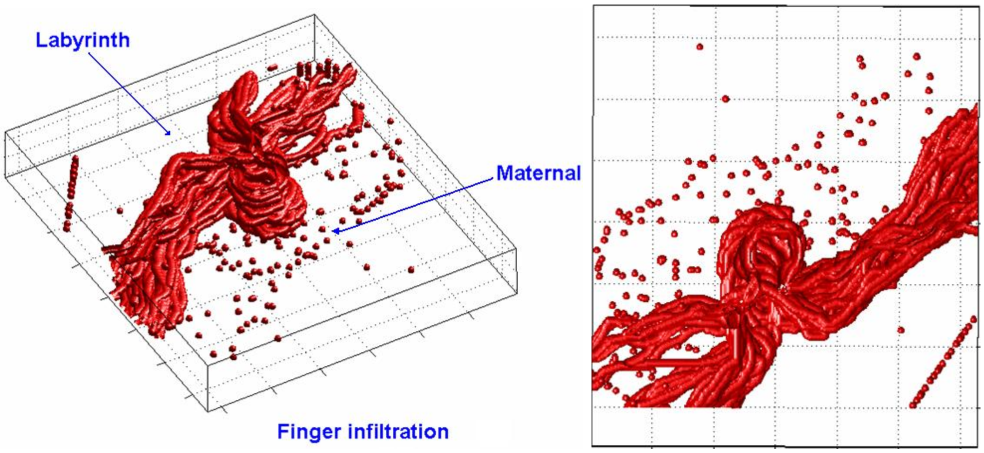

(b) Stream tubes fitted to the finger boundary for visualization

(c) Top view of the infiltration

Figure 10. Visualization of a finger-like infiltration from the spongiotrophoblast into the labyrinth in the 04-2069 registered placenta dataset.

show an improvement in the final 3D reconstructions and overall lower MI metric values. In the future, we will apply our methods to additional histology datasets including those of higher magnifications. Data-structures such as the *kd*-tree will be used to improve efficiency. Deformable models will be explored to account for the shear in the sectioning and mounting stages. This will results in a better quality of alignment and the visualization of fine finger-like infiltrations.

REFERENCES

1. L. Wu, A. de Bruin, H. I. Saavedra, M. Starovic, A. Trimboli, Y. Yang, J. Opavska, P. Wilson, J. C. Thompson, M. C. Ostrowski, T. J. Rosol, L. A. Woollett, M. Weinstein, J. C. Cross, M. L. Robinson, and G. Leone, "Extra-embryonic function of Rb is essential for embryonic development and viability," *Nature* **421**, pp. 942–947, 2003.
2. L. Ibáñez and W. Schroeder, "The ITK Software Guide," *The Insight and Registration Toolkit [www.itk.org], Kitware, Inc.* , 2003.
3. H. Johnson and G. Christensen, "Consistent landmark and intensity based image registration," *In IEEE Transactions on Medical Imaging* **21**, pp. 450–461, 2002.
4. H. Chui, J. Rambo, J. S. Duncan, R. Schultz, and A. Rangarajan, "Registration of cortical anatomical structures via robust 3d point matching," in *IPMI '99: Proceedings of the 16th International Conference on Information Processing in Medical Imaging*, pp. 168–181, 1999.
5. C. Davatzikos, "Spatial transformation and registration of brain images using elastically deformable models," *Computer Vision and Image Understanding* **66**(2), pp. 207–222, 1997.
6. J. P. Thirion, "Fast non-rigid matching of 3D medical images," in *Medical Robotics and computer aided surgery, MRCAS'95*, pp. 47–54, 1995.
7. J. P. Thirion, "Fast non-rigid matching of 3D medical images," in *Computer Vision and Pattern Recognition, CVPR'96*, 1996.
8. J. P. Thirion, "Image matching as a diffusion process: an analogy with maxwell's demons," *Medical Imaging Analysis* **2(3)**, pp. 243–260, 1998.
9. A. Carreras, R. Fernandez-Gonzalez, and C. Ortiz de Solorzano, "Automatic registration of serial mammary gland sections," in *In Proceedings of the 26th Annual International Conference of the IEEE EMBS*, 2004.
10. T. Leung and J. Malik, "Contour continuity in region based image segmentation," *Lecture Notes in Computer Science* **1406**, pp. 544–559, 1998.
11. J. Hsieh, H. M. Liao, K. Fan, M. Ko, , and Y. Hung, "Image registration using a new edge-based approach," *Computer Vision amd Image Understanding* **67(2)**, pp. 112–113, 1997.
12. H. Li, B. Manjunath, and S. Mitra, "A contour-based approach to multisensor image registration," *IEEE Transactions on Image Processing* **56(4)**, pp. 320–334, 1995.
13. S. Ourselin, A. Roche, G. Susol, X. Pennecand, and N. Ayache, "Reconstructing a 3D structure from serial histological sections," *Image and Vision Computing* **19(1)**, pp. 25–31, 2001.
14. P. S. Bradley, U. Fayyad, and C. Reina, "Scaling clustering algorithms to large databases," in *Proceedings of 4th International Conference on Knowledge Discovery and Data Mining (KDD-98)*, pp. 8–15, 1998.
15. F. Maes, A. Collignon, D. Vandermeulen, G. Marchal, and P. Suetens, "Multimodality image registration by maximization of mutual information," *IEEE Trans. Medical Imaging* **16(2)**, pp. 187–198, 1997.
16. P. Viola and W. M. Wells III, "Alignment by maximization of mutual information," in *International Conference on Computer Vision*, pp. 16–23, 1995.
17. J. A. B. Maintz, "Retrospective registration of tomographic brain images," *Ph.D. dissertation, Univ. Utrecht, Utrecht, The Netherlands* , 1996.
18. F. Maes, D. Vandermeulen, and P. Suetens, "Medical image registration using mutual information," *Proceedings of the IEEE* **91(10)**, pp. 1699–1722, 1996.
19. F. Maes, D. Vandermeulen, and P. Suetens, "Comparative evaluation of multiresolution optimization strategies for multimodality image registration by maximization of mutual information," *Medical Image Analysis* **3(4)**, pp. 373–386, 1999.
20. C. Studholme and D. L. G. Hill, "Automated 3-D registration of MR and CT images of the head," *Medical Image Analysis* **1(2)**, pp. 163–175, 1996.